EES Catalysis

PAPER

View Article Online
View Journal

Cite this: DOI: 10.1039/d6ey00058d

NiFeCo-based catalysts in high current zero-gap anion exchange membrane water electrolyzers

B. Milenia Rojas Mendoza,[ab] Ryan T. Hannagan,[abc] Sofia Kimuyu,[a] Colin F. Crago,[ab] Alfred Vargas,[ab] Ashton M. Aleman,[ab] Johanna Schröder,[d] Daniela H. Marin,[ab] Isabela Rios Amador,[ab] Jaehyuk Shim,[ab] Adam C. Nielander,[b] Michaela Burke Stevens*[b] and Thomas F. Jaramillo*[ab]

Understanding degradation mechanisms in pure water anion exchange membrane water electrolyzers is essential for developing durable and precious metal-free hydrogen production systems, yet electronic, chemical, and transport-driven pathways often occur simultaneously at the anode. To separate these effects, we establish a morphology invariant Ni/Fe/Co thin film model catalyst platform using physical vapor deposition and systematically compare composition-dependent behavior under both pure water and 0.1 M KOH feeds. Devices were operated under industrially relevant current density conditions, galvanostatically at 1 A cm^{-2} for 24 hours; metal dissolution, ionomer oxidation, and resistance growth were quantified using inductively coupled plasma mass spectrometry, X-ray photoelectron spectroscopy (XPS), and electrochemical impedance spectroscopy. Under pure-water operation, Ni-rich films showed voltage increases that correlated with rising total cell resistance ($\Delta V \approx 243$ mV, $\Delta R \approx 0.17\ \Omega\ cm^2$). Co-rich films maintained near constant voltages with minimal resistance change ($\Delta V < 10$ mV, $\Delta R \approx 0.03\ \Omega\ cm^2$) but induced pronounced ionomer oxidation observed by XPS. In 0.1 M KOH, ionomer oxidation is suppressed, and impedance growth is minimized ($<0.08\ \Omega\ cm^2$) across all compositions, consistent with reduced transport limitations and improved ionic conduction relative to pure-water feeds. These results demonstrate how a controlled thin film model platform can isolate composition electrolyte relationships and provide mechanistic design principles for stable pure water anion exchange membrane electrolyzers.

Received 18th March 2026,
Accepted 20th March 2026

DOI: 10.1039/d6ey00058d

rsc.li/eescatalysis

Broader context

Green hydrogen produced by renewable-powered electrolysis is central to decarbonizing heavy industry and enabling large-scale energy storage. Among electrolyzer technologies, anion exchange membrane water electrolyzers (AEMWEs) promise the efficiency of proton exchange systems while using earth-abundant catalysts and benign operating conditions. However, instability of both catalysts and ionomers in pure-water-fed devices remains a major obstacle to commercialization. Our work systematically disentangles these degradation pathways by leveraging compositionally controlled NiFeCo thin-film catalysts synthesized *via* physical vapor deposition. This model platform allows us to isolate how catalyst composition and electrolyte feed, such as pure water and 0.1 M KOH, influence electrochemical stability, impedance evolution, and ionomer oxidation. By revealing when and why each degradation mode dominates, this study provides practical design principles for improving both catalyst and ionomer durability, accelerating the transition of AEMWEs from laboratory prototypes to scalable, low-cost green hydrogen systems.

1. Introduction

Renewable electricity is expanding worldwide and has increased the demand for electrochemical technologies that convert intermittent power into storable chemical fuels.[1,2] Hydrogen production through water electrolysis is central to these efforts, but broad deployment requires systems with high durability and low cost.[3,4] Anion exchange membrane water electrolyzers (AEMWEs) have gained interest because they can

[a] *Department of Chemical Engineering, Stanford University, 443 Via Ortega, Stanford, CA 94305, USA*
[b] *SUNCAT Center for Interface Science and Catalysis, SLAC National Accelerator Laboratory, 2575 Sand Hill Road, Menlo Park, CA 94025, USA. E-mail: michaela.burke.stevens@gmail.com, mburkes@slac.stanford.edu, jaramillo@stanford.edu*
[c] *Department of Chemical Sciences, Bridgewater State University, Bridgewater, MA 02325, USA*
[d] *Institute for Chemical Technology and Polymer Chemistry (ITCP), Karlsruhe Institute of Technology (KIT), Engesserstrabe 18, 76131, Karlsruhe, Germany*

operate with earth-abundant catalysts while maintaining the compact zero gap configuration characteristic of proton exchange membrane systems.[5,6] Their compatibility with low alkaline or even pure water feeds reduces system complexity and eliminates the handling of concentrated alkaline solutions.[7,8] At the same time, operation under such low alkalinity conditions exposes the anode to degradation pathways that remain poorly resolved at the mechanistic level, which has hindered the development of stable and precious metal-free catalyst systems.[8]

A major challenge is that degradation in pure water AEMWEs originates from several interconnected pathways that evolve simultaneously within the catalyst ionomer membrane interface.[9–12] Transport limitations inherent to pure water feeds restrict hydroxide availability and increase ionic resistance in both the ionomer and the membrane.[13–15] Specifically, the catalyst undergoes composition-dependent oxidative phase evolution.[16] Under neutral or weakly alkaline feeds, Ni-based catalysts often struggle to form conductive NiOOH and tend to accumulate insulating β-Ni hydroxide, which increases electronic resistance leading to increased cell voltage.[17–19] Co-based catalysts more easily access conductive CoOOH-like surface states, which improve electronic transport and reduce resistance growth.[20] This transport-limited regime suppresses the formation of conductive active phases in Ni-based materials and increases chemical stress at interfaces involving Co-rich catalysts.[21] Moreover, PiperION and related ionomers can undergo oxidative cleavage of the carbon backbone, which has been identified by the formation of carboxyl groups in X-ray photoelectron spectroscopy (XPS).[22,23] High-turnover environments, strong interfacial electric fields, and reactive oxygen species can intensify this process, and chemical degradation can proceed even when the catalyst layer maintains electronic stability.[19,20] Given that these electronic, chemical, and transport-driven pathways occur concurrently and influence one another, previous studies have struggled to determine which mechanisms dominate under pure water conditions.[24]

Most prior investigations have relied on nanoparticle catalysts or electrodeposited films. Although such materials can achieve high performance due to their high surface area to volume ratio, they introduce variability in particle size,[25,26] ink stability,[27–29] porosity,[30] ionomer distribution,[31,32] and metal loading.[33] These additional variables obscure intrinsic compositional effects and complicate mechanistic interpretation.[34,35] To develop generalizable and reproducible insights into pure water degradation, a model catalyst platform that removes morphological ambiguity is necessary.[36]

In this work, we synthesize a morphology-invariant Ni–Fe–Co thin film catalyst platform prepared by physical vapor deposition. This architecture provides continuous metal layers with uniform thickness, consistent surface coverage, and precisely defined composition. Importantly, this fabrication technique enables stable, reproducible operation at high current density in a zero-gap AEMWE architecture under controlled interfaces. By controlling morphology, loading, and roughness, the platform reveals intrinsic composition-dependent behavior under both pure water and alkaline feeds. Through the combined use of galvanostatic impedance spectroscopy, XPS, and inductively coupled plasma mass spectrometry (ICP-MS), we separate resistance, chemically, and transport-driven contributions to voltage rise. Our results show that Ni-rich films degrade primarily through resistance-driven pathways, while Co-rich films retain electronic stability but induce more ionomer oxidation. The introduction of dilute KOH suppresses ionomer degradation and minimizes resistance growth across all catalysts. These findings establish composition electrolyte relationships that connect catalyst phase evolution, ionomer chemistry, and transport limitations and provide a composition-dependent, evidence-bounded framework for the design of durable pure water AEMWEs.

2. Results and discussion

2.1. Fine-tuning tri-metallic anode catalyst coatings

A key challenge in evaluating electrocatalyst materials is that compositional changes are often accompanied by changes in other factors, such as morphology[37] and conductivity.[38] Here, we address this issue by using electron beam physical vapor deposition (PVD) to achieve uniform and reproducible metallic coatings across samples, as shown in Fig. 1a. To isolate the role of composition, five different catalysts were deposited onto a stainless-steel porous transport layer (PTL): Ni_{100}, Co_{100}, $Ni_{81}Fe_{19}$, $(Ni_{81}Fe_{19})_{90}Co_{10}$, and $(Ni_{81}Fe_{19})_{10}Co_{90}$, where the subscript is the atomic percentage. For simplicity, throughout this paper, we refer to Ni_{100} as Ni, Co_{100} as Co, $Ni_{81}Fe_{19}$ as Ni/Fe, $(Ni_{81}Fe_{19})_{90}Co_{10}$ as $(Ni/Fe)_{90}Co_{10}$, and $(Ni_{81}Fe_{19})_{10}Co_{90}$ as $(Ni/Fe)_{10}Co_{90}$.

X-ray photoelectron spectroscopy (XPS) depth profiling was performed to evaluate oxidation state and elemental distribution in the thin films (Fig. S1). In the Ni and Ni/Fe-rich films, the Ni 2p spectra displayed a peak position at 853.7 eV, which is characteristic of NiO, while the metallic Ni signal increased at greater depths (852.6 eV).[39] Depth profiling also quantified the atomic % (at%) of Ni, Fe, and Co extracted from the Fe 3p peak as a function of sputter time for all three alloys, demonstrating that each film maintains its target composition (±15%) throughout the ~100 nm nominal thickness (Fig. S1).

Grazing-incidence X-ray diffraction (GIXRD) was used to characterize the crystallinity and alloying of the thin films (Fig. S2). The Ni film exhibited a sharp peak at 2θ = 19.9°, which corresponds well with the face-centered cubic (FCC) Ni reference pattern (ICSD #125671). The Ni/Fe film XRD showed a peak at 2θ = 20.3°, between the corresponding peaks of the FCC Ni peak (19.9°) and the body-centered cubic (BCC) Fe peak (20.4°) (ICSD #14754), indicating alloying. By contrast, the Co-rich films displayed broader peaks centered at 2θ = ~18–21°, which align with the hexagonal close-packed (HCP) Co standard (ICSD #36677), though significant broadening suggests reduced crystallite size and/or partial structural disorder. The intermediate alloys, $(Ni/Fe)_{90}Co_{10}$, and $(Ni/Fe)_{10}Co_{90}$, showed peak positions between those of the Ni and Co standards,

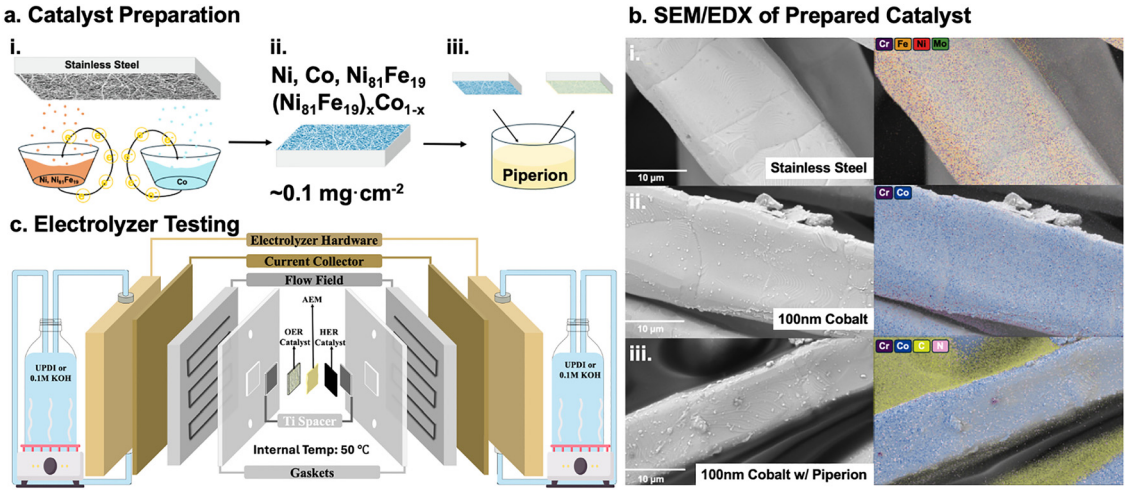

Fig. 1 Uniform thin-film catalyst fabrication, characterization, and electrolyzer assembly. (a) Process flow for anode catalyst preparation: (i) electron beam induced physical vapor deposition of Ni_{100}, Co_{100}, $Ni_{81}Fe_{19}$, $(Ni_{81}Fe_{19})_{90}Co_{10}$, and $(Ni_{81}Fe_{19})_{10}Co_{90}$ alloys onto a stainless steel porous transport layer (PTL) to achieve ~0.1 mg cm^{-2} loading; (ii) resulting loading of ~0.1 mg cm^{-2}, corresponding to a 100 nm thick metal thin film; (iii) dip-coating of the coated PTL into 2 wt% PiperION, resulting in a ~1 mg cm^{-2} ionomer overlayer. (b) SEM images (left) and corresponding SEM EDX elemental maps (right) of (i) bare stainless steel PTL, (ii) 100 nm Co film on PTL, and (iii) the same Co film after ~1 mg cm^{-2} PiperION dip-coating. (c) Schematic cross-section of the zero-gap membrane electrode assembly: PTLs with dip-coated anode (OER catalyst), spray-coated Pt/C cathode (HER catalyst), and the PiperION AEM; liquid feed (DI water or 0.1 M KOH) is circulated through separate anode and cathode reservoirs, and the cell was maintained at 50 °C.

indicating partial alloying rather than complete phase segregation. To avoid over-assignment, these XRD results were interpreted as qualitative evidence of alloying and disorder rather than definitive phase identification.

To evaluate the elemental homogeneity of the thin film deposition onto a PTL, scanning electron microscopy coupled with energy-dispersive X-ray spectroscopy (SEM-EDX) was used to map the electrode surface compositions at each stage of preparation. SEM-EDX analysis of the bare stainless steel PTL surface exhibited predominantly Fe (~65 at%) and Cr (~22 at%), with a smaller amount of Ni (~12 at%) and Mo (~1 at%) (Fig. 1b(i)). After Co catalyst deposition, SEM-EDX mapping (Fig. 1b(ii)) showed that the Co is conformally deposited across the porous stainless steel PTLs. EDX surface analysis of the monometallic Co film revealed a composition of ~92 at% Co and ~8 at% Cr, with no Fe detected, indicating that the Co film forms a nearly continuous layer that fully covers the stainless-steel substrate in the analyzed region. Ni, Ni/Fe, and (Ni/Fe)Co films showed qualitative effective coverage throughout the PTL (SI Fig. S3). Following the thin film deposition, the anode side of the PTL was dip-coated in a PiperION solution, resulting in an ionomer overlayer of approximately 1 mg cm^{-2} on the electrode.

Fig. 1b(iii) shows the catalyst with the ionomer overlayer, as evidenced by C and N detection in the SEM–EDX, which revealed 72 at% of C, 1 at% of N, 2 at% of Cr, and 25 at% of Co, indicating ionomer coverage on the PTL surface and within the strands. SEM–EDX detected only N, while F was not observed, consistent with EDX detection limitations. In contrast, strong F and N peaks, along with suppression of metallic signals in the XPS of the pre-echem catalysts of the coated PTLs, confirmed uniform ionomer coverage across all samples (SI Fig. S7). This XPS evidence supports treating SEM-EDX elemental maps as qualitative indicators of coverage rather than quantitative ionomer composition.

The anode catalysts, together with a Pt/C cathode spray-coated onto Toray paper, were assembled into an AEMWE using a PiperION membrane (Fig. 1c). Electrochemical testing was conducted using either deionized water (DIW) or 0.1 M KOH as the feed for both the anode and cathode. Overall, these analyses confirmed that the PVD-fabricated thin film catalysts maintain controlled composition, uniform morphology, and consistent ionomer coverage across samples, providing a well-defined platform to evaluate electrochemical performance under different electrolyte conditions.

2.2. AEMWE performance comparison under DIW feed conditions

The uniformly coated and characterized PTLs were assembled into the AEMWE cell (Fig. 1) to assess their electrochemical performance. The cell underwent a conditioning break-in phase, following the published literature for AEMWE performance.[13,40] During which it was operated at progressively increasing current densities (SI Fig. S4). This is hypothesized to hydrate the membrane and ionomer and stabilize ionic conductivity before performance measurements.[24] Following this conditioning step, polarization curves were recorded to assess the initial performance of each catalyst (Fig. 2a).

The thin film catalysts exhibited similar initial performance at 1 A cm^{-2} at the beginning-of-life (BOL) (Fig. 2a), with operating potentials spanning from 2.30–2.36 V 1 A cm^{-2}. This range suggests that composition-dependent differences in catalyst activation are minimal under initial operating conditions in DIW. However, IrO_x nanoparticles (nps), used as a form

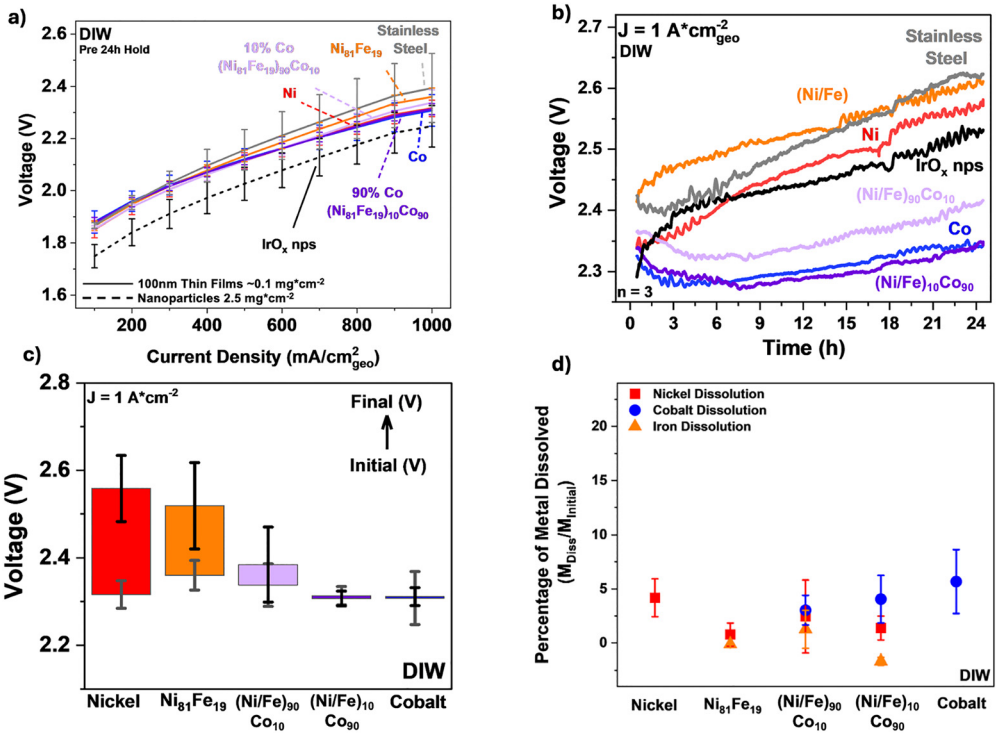

Fig. 2 Performance, stability, and metal dissolution of thin-film anode catalysts in DIW-fed AEMWE cells. All data shown as averages from triplicate measurements (n = 3), with error bars representing one standard deviation from the mean. (a) Polarization curves collected after break-in, prior to the 24 h hold at j = 1 A cm^{-2}, Beginning of life (BOL). (b) Voltage as a function of time profiles at 1 A cm^{-2} over 24 h. From the average of triplicates (c) Initial (BOL) and end of life (EOL) voltages at 1 A cm^{-2} extracted from pol curves. (d) Percentage of metal dissolved after 24 h electrolysis (EOL), as quantified by ICP-MS, where negative values reflect that the measurement was below the detection limit.

of reference, exhibited the best performance overall (2.24 V at 1 A cm^{-2}), whereas the bare stainless-steel substrate alone showed marginally worse performance (2.39 V at 1 A cm^{-2}). Although the thin film catalysts exhibited similar BOL performance, differences in electrochemical stability, defined as the rate of cell voltage change during galvanostatic operation, emerged during the 24-hour stability test in DIW (Fig. 2b). The Ni sample displayed a nearly linear increase in cell voltage, with an average degradation rate of 8.9 mV h^{-1}. In contrast, the Ni/Fe sample began and ended at a higher voltage than Ni but showed an average slower degradation rate of 6.9 mV h^{-1}. During the galvanostatic hold, the Co-containing samples showed a decrease in voltage during the first 6–8 hours. For instance, Co performance improved at a rate of 2.9 mV h^{-1}, $(Ni/Fe)_{90}Co_{10}$ at 11.9 mV h^{-1}, and $(Ni/Fe)_{10}Co_{90}$ at 8.1 mV h^{-1}. After this 9-hour period, a steady, linear degradation trend emerged. As a result, we calculated the degradation rates for these samples starting from the 9-hour mark. The degradation rates were on average 5.5 mV h^{-1} for $(Ni/Fe)_{90}Co_{10}$, 5.3 mV h^{-1} for $(Ni/Fe)_{10}Co_{90}$, and 3.9 mV h^{-1} for pure Co.

Fig. 2c summarizes the voltage increase for each catalyst during the 24-hour stability test at a constant current density of 1 A cm^{-2}. The Ni electrode exhibited the largest voltage increase (240 mV ±10 mV) during the 24-hour stability test. This voltage increase is consistent with the formation of less-conductive Ni hydroxide-like species (for example β-$Ni(OH)_2$) under these operating conditions, which could increase electrode resistance and decrease electrochemical activity due to conductivity limitations, resulting in a higher operating voltage.[41–43] Ni/Fe showed the second-worst performance loss, with a 159 mV ± 13 mV increase. Nonetheless, this suggests that incorporating Fe into Ni improves stability when compared to monometallic Ni. However, prior studies in pure-water and dilute-alkalinity AEMWE environments have frequently shown that Fe incorporation can destabilize Ni-based catalysts. Previous literature reported that Ni–Fe systems often undergo rapid conversion and instability under low-alkalinity conditions due to Fe-facilitated phase evolution into oxyhydroxides.[21,38] In contrast, in our thin-film platform, the $Ni_{81}Fe_{19}$ catalyst, while still degrading substantially in DIW, does not destabilize as severely as expected from nanoparticle or electrodeposited Ni–Fe systems. This improved stability may be related to the controlled thin-film geometry: the rate of conversion from the Ni–Fe metal to its oxyhydroxide phases, along with the difference in stability between the bulk metal and bulk oxyhydroxide layers, could mitigate the destabilizing effects commonly reported for Ni–Fe combinations.

In contrast, the Co-containing samples exhibited lower net voltage changes: 47 mV ± 13 mV for $(Ni/Fe)_{90}Co_{10}$, 6.3 mV ± 2 mV for $(Ni/Fe)_{10}Co_{90}$, and 3.3 mV ± 8 mV for pure Co. These results show that electrochemical stability improves with increasing Co

content in the thin-film platform under DIW-fed AEMWE conditions.

To determine whether metal dissolution contributed to the observed electrochemical degradation, anolyte aliquots were analyzed with ICP-MS (Fig. 2d) to quantify the amount of metal dissolved after 24 hours.

To confirm that the observed Ni dissolution was not primarily originating from the stainless-steel substrate, control experiments run under the same conditions were conducted using bare stainless steel PTLs, and aliquots were analyzed by ICP-MS. Fig. S6 provides the raw ICP-MS dissolution data (Ni, Co, and Cr) for all samples, including a bare stainless-steel control. Cr dissolution from the stainless-steel control defines an upper bound for PTL contributions under DIW conditions. The catalyst-coated samples show negligible Cr signals, indicating that PTL remains intact and does not dissolve during operation. Values near the ICP-MS detection limit are treated as negligible and are reported with associated uncertainty. The Ni concentration contributed by the stainless steel was approximately 1000 ng, which corresponds to $\sim$1 ppb when normalized to the 1 L anolyte volume (Fig. S6). This value was used as a baseline correction for DIW-fed experiments and was subtracted from subsequent measurements to better isolate Ni dissolution attributable to the catalyst layer. By calculating the percentage of dissolved metal relative to the initial metal content, we found that the Ni sample exhibited $\sim 4.1 \pm 2\%$ Ni dissolution, while the Co sample showed a similar value of $\sim 5.6 \pm 3\%$ Co dissolution. Despite their vastly different electrochemical stability and performance, both metals leached at comparable levels.

Interestingly, even after normalizing to the percentage of Ni present in the film, the Ni/Fe alloy showed reduced Ni dissolution, dropping from 4% to $1 \pm 1\%$, from Ni to Ni/Fe, respectively. When Co was introduced, Ni dissolution increased compared to the Ni/Fe sample, rising to approximately $2.4 \pm 3\%$ in the $(Ni/Fe)_{90}Co_{10}$ sample and $1.3 \pm 1\%$ in the $(Ni/Fe)_{10}Co_{90}$ sample, even though there were lower amounts of Ni present in the sample. These results suggest that Co may be associated with Ni dissolution when mixed with the Ni/Fe alloy. This may be due to composition-dependent structural evolution that creates pathways for Ni leaching,[35] or because of Co dissolution, destabilizing the local structure and mobilizing Ni with it. Accordingly, we frame this trend as a correlation rather than a definitive mechanism.

Overall, these findings demonstrate that while initial performance is comparable across thin films, electrochemical degradation is strongly material dependent, highlighting the importance of long-term performance characterization. Co incorporation into Ni/Fe catalysts substantially improves voltage stability in DIW, despite similar dissolution levels across metal types. These results highlight the importance of catalyst composition and structure in long-term performance in AEMWE systems operating with DIW feeds. This decoupling of dissolution and performance highlights that stability in DIW is not solely dictated by material loss to the effluent during short-term stability assessment, and material loss may often not be consistent over time.[44–46] Instead, changes in the catalyst–ionomer interface or surface oxidation states could be causing the observed degradation due to oxidative degradation of the ionomer or dynamic shifts in surface metal oxidation states that alter activity.[7,39]

2.3. Deconvoluting ionomer oxidation and resistance contributions to degradation in DIW

To investigate the contributions of ionomer oxidation and degradation on the anode, we used XPS, as demonstrated in prior studies.[22,38,47] Galvanostatic electrochemical impedance spectroscopy (GEIS) was also employed to monitor changes in the cell resistance during operation. Together, these complementary techniques help deconvolute the respective contributions of ionomer oxidation and resistance increase to overall performance degradation.

To examine anode ionomer oxidation with XPS, we focus on the C 1s region (Fig. 3a), as oxidation of the carbon backbone is a known contributor to device failure.[4] The presence of distinct binding energy features associated with oxidized ionomer species of the carbon backbone allows us to distinguish chemical changes in the ionomer from the substrate signal, such as C═O bonds formed when the benzene ring of the PiperION cleaves and creates a carboxyl group.[22,48] The C 1s spectra were deconvoluted into a set of carbon signals based on expected C 1s binding energy components (C═C, C–O, C═O, C–N, C–F_3). In particular, we tracked the 'C═O' signal, as the emergence of a peak around 288–289 eV corresponds to the formation of carboxyl groups, consistent with backbone cleavage.[22,23,49] This signal was therefore used as a proxy for ionomer oxidation. Minimal C═O signal was detected in the pristine samples. Raw XPS spectra (C 1s, O 1s, F 1s, N 1s) for all samples, including stainless-steel and IrO_x references, are provided in Fig. S7. After electrochemical testing, the C═O content increased substantially, especially for Co ($\sim$25 at%), $(Ni/Fe)_{10}Co_{90}$ ($\sim$23 at%), $Ni_{81}Fe_{19}$ ($\sim$9 at%), and Ni ($\sim$8 at%) relative to the C 1s components. In contrast, the $(Ni/Fe)_{90}Co_{10}$ sample showed only a C═O content increase to $\sim$6%. Stainless steel shows comparatively weaker oxidation features despite operating at higher voltages, reinforcing that ionomer oxidation alone does not uniquely determine short-term voltage rise under DIW operation.

This trend suggests a tradeoff, where higher Co content results in increased ionomer oxidation, even though Co-rich samples show improved electrochemical performance. Prior work reported a similar relationship using nanoparticles, where materials with higher electronic conductivity also exhibited more ionomer oxidation while still maintaining strong performance.[38] Together with our results, these observations may suggest that Co-rich films may sustain more electrochemically active sites during operation. We hypothesize that increased electronic conductivity in the Co-rich catalysts may enable more facile electron transport through the catalyst layer, which may support a broader distribution of OER-active regions at the catalyst–ionomer interface. If more

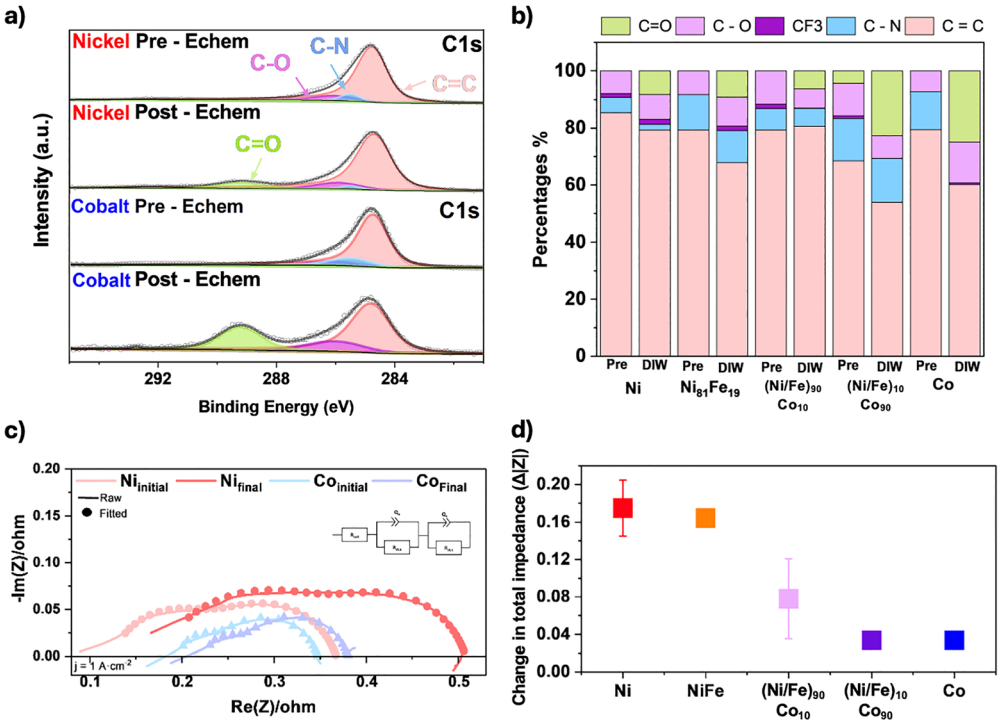

Fig. 3 XPS and resistance measurements of Ni and Co thin film anodes before and after 24 h of electrochemical conditioning. (a) C 1s XPS spectra and peak fits for Ni (top two) and Co (bottom two) samples as deposited before any electrochemical procedures ("Pre-Echem") and after the 24 h galvanostatic hold at 1 A cm^{-2} in DIW ("Post-Echem"), showing deconvolution into C═C, C–N, C–O, CF_3 and C═O components. (b) Percent contribution of each C 1s component (C═C, C–N, C–O, CF_3, C═O) for Ni, $Ni_{81}Fe_{19}$, $(Ni/Fe)_{90}Co_{10}$, $(Ni/Fe)_{10}Co_{90}$, and Co, before (Pre) and after (DIW) electrolysis. (c) Nyquist plots of raw (solid lines) and fitted (dotted lines) GEIS data at 1 A cm^{-2} for initial (lighter markers) and final (darker markers) states of Ni (red) and Co (blue) electrodes. The inset shows the equivalent circuit model used for fitting. (d) Change in total impedance ($\Delta|Z|$) between initial and final EIS measurements (eqn (1)) for each composition, highlighting the smaller increase in resistance with higher Co content.

interfacial regions participate in OER, a greater fraction of the ionomer could be exposed to oxidative local environments, consistent with increased ionomer oxidation features. At the same time, the larger number of active sites helps maintain overall catalyst utilization and therefore preserves electrochemical performance, even as the ionomer undergoes more oxidation.

To assess how catalyst composition influences interfacial processes during operation, we performed GEIS. This technique resolves the high-frequency resistance encompassing membrane and ionomer conductivity, the charge-transfer resistance associated with OER and HER kinetics at the catalyst–ionomer interface, and the interfacial capacitance linked to electrochemically active surface area, thereby capturing the evolution of catalyst–ionomer interactions over time. GEIS was conducted before and after the 24-hour hold at 1 A cm^{-2} to evaluate the change in resistance of each catalyst. A modified Randles circuit model commonly used for AEMWE was employed[50] (Fig. 3c). R_{cell} represents the series resistance of the cell, $R_{ct,a}$ corresponds to the charge transfer resistance of the anodic reaction, and $R_{ct,c}$ represents the charge transfer resistance of the cathodic reaction. To quantify changes in impedance over time, we subtracted the pre-stability hold total resistance values obtained from the GEIS from the post-stability measurements using eqn 1 to obtain the change in total impedance of the cell before and after the 24-hour electrochemical stability hold (Fig. 3d).

$$(R_{cell} + R_{(ct,a)} + R_{(ct,c)})_{EOL} - (R_{cell} + R_{(ct,a)} + R_{(ct,c)})_{BOL} = \Delta|Z| \quad (1)$$

The Ni sample showed an increase in total impedance of approximately 0.17 Ω cm^2, and the Ni/Fe sample exhibited a similar rise of ~0.16 Ω cm^2. During the 24-hour stability hold, the resistance increased, which may reflect limited formation of conductive oxyhydroxide phases under neutral electrolyte feed conditions consistent with prior reports under low alkaline conditions.[51,52] Because all samples begin as metallic thin films, differences in impedance are likely linked to variations in the rate and extent of metal-to-oxyhydroxide conversion. This could be due to Ni only partially converting to active oxyhydroxide phases under pure-water conditions. Instead, it may have partially converted to the more insulating $Ni(OH)_2$ phase.[18,43]

In contrast, all Co-containing samples exhibited smaller changes in total impedance: 0.07 Ω cm^2 for $(Ni/Fe)_{90}Co_{10}$, 0.03 Ω cm^2 for $(Ni/Fe)_{10}Co_{90}$, and 0.03 Ω cm^2 for monometallic Co. This trend indicates enhanced conductivity stability during the hold period compared to the Ni samples, potentially due to reported higher electronic conductivity of Co-containing oxide/oxyhydroxide phases relative to Ni hydroxide-like phases.[52–55]

Interestingly, even though Co-rich electrodes promote ionomer oxidation, which would be expected to hinder ionic conductivity, we observe a stable total cell resistance and electrochemical performance. This suggests that the higher electronic conductivity and catalytic activity of Co-based oxides may offset the negative effects of ionomer degradation. We note that this is a correlation-based interpretation rather than a direct identification of specific oxide phases, since *operando* phase tracking was not performed. This motivates additional studies involving *operando* techniques.

Previous studies on nanoparticle-coated electrodes have shown that more conductive catalysts such as IrO_x and Co_3O_4 promote uniform OER activity throughout the catalyst layer, even though this can accelerate ionomer oxidation.[38,51] Our thin-film platform exhibits a similar overall trend: the Co metal films maintain stable electronic conductivity during operation, which helps prevent large increases in resistance even when some ionomer degradation occurs. In contrast, the Ni-rich films show a larger rise in total resistance. Under pure-water conditions, Ni does not fully access its more conductive phases, consistent with prior reports that Ni activation is limited in low-alkalinity feeds.[21,38,51] This limited activation likely contributes to the larger resistance increases observed for Ni and Ni/Fe samples. Together, these results indicate that ionomer oxidation alone cannot account for performance loss in DIW; resistance growth plays a dominant role. To further separate these contributions, we next examine catalyst behavior in 0.1 M KOH, where higher ionic conductivity stabilizes the catalyst–ionomer interface.

2.4. Electrochemical performance and degradation in 0.1 M KOH

Prior studies have reported that introducing a supporting electrolyte, such as KOH, can suppress membrane and ionomer oxidation by stabilizing ionic conductivity through enhanced OH^- transport and reducing oxidative stress on the polymer matrix.[22,56,57] To probe this, we conducted experiments using 0.1 M KOH feed to both the anode and cathode. The goal was to provide a more chemically stable environment and enable clearer separation between electrical resistance-driven degradation and chemically induced ionomer damage. This approach allows us to assess the electrochemical performance of the catalysts under improved ionic transport conditions and to better isolate the contributions of catalyst, ionomer, and membrane stability to overall device performance.

Fig. 4a shows the initial and final voltages at 1 A cm^{-2} in DIW (solid bars) and in 0.1 M KOH (hatched bars). Notably, the Ni and Ni/Fe electrodes, which previously showed significant voltage increases in DIW (243 mV and 159 mV over 24 h at j = 1 A cm^{-2}, respectively), exhibited improved electrochemical stability in 0.1 M KOH over 24 h (61 mV and 64 mV over 24 h at j = 1 A cm^{-2}, respectively). Although the catalyst–ionomer interface is locally alkaline in both DIW and KOH operation, the presence of a bulk hydroxide electrolyte provides additional ion-transport pathways and reduces transport limitations relative to DIW feeds.[58]

The alkaline environment may support more complete conversion of Ni to more conductive oxyhydroxide-like surface states,[59] leading to reduced voltage changes. In contrast, the Co-rich samples exhibited the opposite trend; although the Co-rich samples maintained lower absolute voltages than in DIW, their voltages increased more over the 24-hour stability hold, indicating greater degradation under 0.1 M KOH. The $(Ni/Fe)_{90}Co_{10}$ sample remained relatively unchanged (47 mV in DIW versus 56 mV in KOH), while the $(Ni/Fe)_{10}Co_{90}$ sample, which initially only increased by 6 mV in DIW, degraded by 42 mV in KOH. Most notably, the pure Co sample showed minimal degradation in DIW (3 mV) but exhibited a 71 mV voltage increase in KOH. This is consistent with previous reports that, although Co-based catalysts perform better in DIW, Ni-based catalysts outperform them in alkaline conditions.[51]

To further investigate the effects of KOH on ionomer degradation, we performed XPS analysis of the C 1s region before and

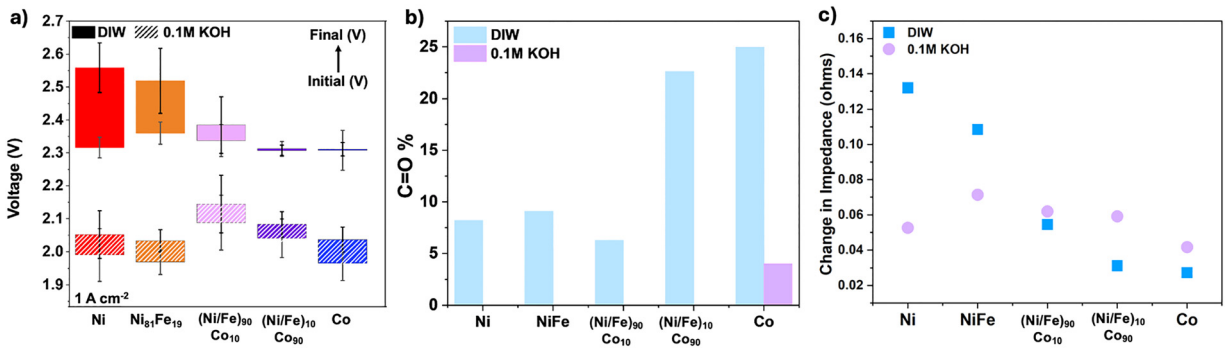

Fig. 4 Effect of 0.1 M KOH *vs.* DIW feed on AEMWE performance, ionomer oxidation, and impedance changes. (a) Box plots of initial (solid fill) and final (hatched fill) voltages at j = 1 A cm^{-2} for Ni, $Ni_{81}Fe_{19}$, $(Ni_{81}Fe_{19})_{90}Co_{10}$, and $(Ni_{81}Fe_{19})_{10}Co_{90}$, illustrating the dramatic reduction in voltage drift for Ni-based catalysts in alkaline feed. (b) Comparison of C═O (%) from C 1s XPS pre- and post-electrolysis in DIW (blue) and 0.1 M KOH (purple), showing severe ionomer oxidation in DIW that is largely suppressed in KOH so much that the C═O present was below the detection limits of the XPS. (c) Change in total cell impedance ($\Delta|Z|$) between initial and final GEIS measurements in DIW (blue squares) and 0.1 M KOH (purple circles), highlighting smaller impedance changes under alkaline conditions.

after electrolysis (Fig. 4b). In DIW, all samples showed a notable increase in carboxyl (C═O) content, particularly in Co-rich electrodes, where C═O rose from ~0 at% to 25 at% for Co and 22.6 at% for $(Ni/Fe)_{10}Co_{90}$, indicating severe oxidative degradation of the ionomer. In contrast, in 0.1 M KOH, C═O content was suppressed to <4 at% across all compositions, with most samples showing no detectable signal, suggesting that the ionomer backbone remained largely intact for all samples.

GEIS was used to quantify changes in total cell resistance following the 24-hour galvanostatic hold at 1 A cm^{-2} (Fig. 4c). While all electrocatalysts exhibited some changes in cell resistance, the magnitude and direction of these changes were not strongly correlated to catalyst composition. For example, Ni showed a decrease in total cell resistance, a change from increasing resistance by 0.17 Ω cm^2 in DIW to a smaller increase of 0.05 Ω cm^2 in 0.1 M KOH, while Co exhibited a small change in impedance, with 0.04 Ω cm^2 in DIW decreasing to 0.03 Ω cm^2 in 0.1 M KOH. Similarly, total cell resistance remained relatively stable across samples, shifting by less than 0.08 Ω cm^2 in KOH, compared to larger swings observed in DIW. These smaller resistance changes in KOH reinforce the stabilizing role of the alkaline environment on the electrode–ionomer interface. Similar trends have been reported in the literature, where higher pH led to minimal changes in total cell resistance across catalysts.[51]

Utilizing 0.1 M KOH as a supporting electrolyte impacts catalyst stability and performance. Ni-based electrodes, which showed significant voltage increase and ionomer degradation in DIW, became much more stable in KOH, possibly due to stabilization of different pH-stable active phases and/or suppressed ionomer oxidation. In contrast, the performance of Co-rich electrodes, despite their strong performance in DIW, degraded more in 0.1 M KOH, consistent with increased susceptibility of Co-rich electrodes to oxidative transformation under more alkaline operation.[60] However, because this study does not include *operando* structural or valence-state measurements, this interpretation remains a correlation-based hypothesis rather than a direct mechanistic assignment. *Ex situ* XPS confirmed reduced ionomer oxidation in alkaline conditions across all samples, while GEIS showed smaller cell resistance changes, indicating improved impedance stability (Fig. 4b and c). Together, these results suggest that introducing a small amount of KOH helps isolate intrinsic catalyst behavior by minimizing ionomer degradation and stabilizing ionic transport, allowing composition-dependent trends to be more clearly observed.

2.5. Correlating ionomer oxidation and resistance buildup with electrochemical degradation

To summarize the observed trends in ionomer oxidation, total cell resistance changes, and electrochemical stability, we directly correlated the change in voltage at 1 A cm^{-2} with both the change in total cell resistance and the degree of ionomer oxidation (measured *via* C═O percentage from post-mortem XPS). These relationships are plotted for DIW (Fig. 5a) and 0.1 M KOH (Fig. 5b), with color maps representing the extent of ionomer oxidation.

In DIW, samples with higher resistance changes also showed greater change in voltage but minimal ionomer oxidation. For example, the Ni electrode exhibited the highest voltage increase (243 mV), the highest cell resistance change (0.17 Ω cm^2), but had low ionomer oxidation with 8.1% C═O present. Similarly, Ni/Fe increased by 159 mV with a 0.11 Ω cm^2 resistance increase, but also had low ionomer oxidation with only 6.5% C═O. In contrast, Co-rich samples showed much lower resistance changes and smaller voltage shifts despite more pronounced ionomer oxidation. The pure Co sample, for instance, exhibited only 3.4 mV voltage increase and 0.027 Ω cm^2 resistance increase, but had the highest C═O signal (25.3%). This suggests that in DIW, electrochemical degradation is driven primarily by electronic resistance changes of the catalyst, while ionomer oxidation does not substantially dictate overall electrochemical performance loss.

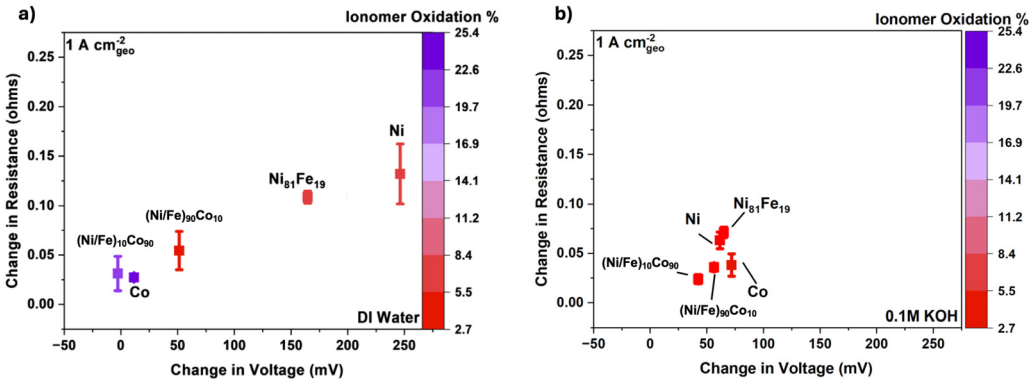

Fig. 5 Correlation of electrochemical degradation, impedance rise, and ionomer oxidation for thin-film anode catalysts at 1 A cm^{-2}. (a) DIW feed: each point represents a catalyst composition (Ni, $Ni_{81}Fe_{19}$, $(Ni/Fe)_{90}Co_{10}$, and $(Ni/Fe)_{10}Co_{90}$, Co), plotted by voltage increase (ΔV) *versus* total resistance increase (ΔR) over 24 h, with marker color indicating post-mortem C═O content (%) from XPS. In DIW, ΔV scales with ΔR despite large variations in ionomer oxidation. (b) 0.1 M KOH feed: the same metrics show overall lower ΔV, smaller ΔR, and suppressed ionomer oxidation (<5% C═O) for all compositions under alkaline conditions.

In 0.1 M KOH, the relationships break down. Impedance changes fall within a narrow range across all samples (0.03–0.08 Ω cm^2), and ionomer oxidation is negligible, with carboxyl (C═O) content below 5 at% for every composition. Despite this uniformity in interfacial properties, we still observe variations in voltage changes. Ni and Ni/Fe showed similar electrochemical stability with an increase of 61 mV and 64 mV, respectively, while $(Ni/Fe)_{90}Co_{10}$, $(Ni/Fe)_{10}Co_{90}$, and Co increased by 56 mV, 42 mV, and 72 mV, respectively. Notably, the intermediate compositions $(Ni/Fe)_{10}Co_{90}$ and $(Ni/Fe)_{90}Co_{10}$ exhibit the smaller net changes in both voltage and resistance under 0.1 M KOH, whereas Co shows the largest voltage drift (72 mV) despite similarly small ΔR (0.04 Ω cm^2). This suggests that under alkaline feed, ionomer oxidation is strongly suppressed, and impedance growth is minimized. As a result, performance changes are likely driven by multiple coupled factors, including composition-dependent interfacial kinetics and surface transformation, in addition to potential changes in both ionic and electronic resistance.

In contrast, the supporting electrolyte may promote both ionic and chemical stabilization in Ni-based catalysts, possibly by facilitating access to more conductive oxyhydroxide-like surface states under alkaline operation, thus leading to lower voltage changes. Small changes in ΔV in KOH, even when ΔR and C═O are lower, indicate that voltage increase is not uniquely determined by either total resistance growth or ionomer oxidation alone under these conditions. Although catalyst layers have identical thickness and nominal loading, the electrochemically active surface area (ECSA) and intrinsic site density may differ across compositions due to differences in crystallinity and surface transformation behavior. Because this work focuses on decoupling degradation modes under controlled morphology rather than on quantifying intrinsic activity (ECSA or TOF), we do not interpret stability trends as direct functions of active-site density. Future work combining this platform with independent ECSA or TOF normalization could test whether the observed KOH trends persist after accounting for active site density.

Together, these comparative plots highlight the complex interplay between electrochemical, physical, and chemical degradation pathways in AEMWE systems. In DIW, performance degradation is strongly correlated with increases in total cell impedance, unrelated to ionomer oxidation, and is highly composition-dependent. In contrast, 0.1 M KOH largely suppressed these degradation modes, resulting in more uniform and stable operation across all catalyst compositions with low total impedance cell changes (<0.09 Ω cm^2), suppressed ionomer oxidation ($<4\%$ C═O), and smaller voltage changes across all samples ($<$ 10 mV differences).

3. Conclusion

In this work, we established a uniform platform to evaluate catalyst composition effects in AEMWEs by standardizing catalyst loading and morphology. Thin film anodes (100 nm, ~0.1 mg cm^{-2}) were fabricated by e-beam physical vapor deposition to ensure surface area and particle size, enabling direct comparison of intrinsic catalyst behavior under high-current operation. Using a combination of XRD, XPS, ICP-MS, and GEIS, we identified correlations between catalyst resistance evolution, ionomer oxidation, and electrochemical stability.

Increasing Co content in the anode $(Ni_{81}Fe_{19})_{90}Co_{10}$ < $(Ni_{81}Fe_{19})_{10}Co_{90}$ < Co improved electrochemical stability during 1 A cm^{-2} for a 24 h galvanostatic operation. This is likely consistent with Co-rich samples maintaining a relatively stable total cell resistance; however, this stability correlated with greater ionomer oxidation at the catalyst–ionomer interface, as shown in Fig. 6, potentially because the Co-rich anodes preserved electronic conductivity, possibly enabling higher electron transport and increased active sites and interfacial interactions between the catalyst and ionomer in DIW feeds.[54,61] In contrast, Ni and $Ni_{81}Fe_{19}$ samples, due to the possible low presence of OH^-, have little electrical and chemical driving force at the interface to access their more active pH-dependent states. This may result in a more insulating catalyst layer, causing electronic resistance to increase over time and reducing the number of active sites between the anode catalyst and ionomer interface, therefore leading to less ionomer oxidation as shown in Fig. 6. To mitigate ionomer oxidation, we introduced 0.1 M KOH as a supporting electrolyte. In this environment, resistance changes were suppressed across all tested compositions. However, Co-rich samples exhibited greater electrochemical degradation relative to Ni-based films, consistent with oxidative transformation of Co-rich catalysts under more alkaline operation, while Ni-based samples showed improved electrochemical stability, presumably due to enhanced conversion to the active phase facilitated by the higher alkalinity. These findings showed how a controlled thin-film model platform can isolate composition–electrolyte relationships and provide evidence-based design hypotheses for stable pure-water and alkaline AEM electrolyzers. We developed a framework that links resistance evolution, ionomer oxidation, and composition-dependent stability. Future work can build on this platform by integrating *operando*, high-current diagnostics (for example, *operando* XAS[62]) under both DIW and dilute-alkaline feeds to directly assign evolving oxidation states/phases and to validate the correlations observed here under operating conditions. This work provides a framework for the advancement of industrially relevant green hydrogen production essential for a fossil fuel-independent future.[63]

4. Experimental methods

4.1. Electrode synthesis

4.1.1. Cathode preparation. Cathodes were fabricated by spray coating catalyst ink onto a carbon-based PTL with an ultrasonic spray coater (Sonotek Spray coater). All cathode inks were prepared by mixing Pt on carbon 5% (0.2 g) [Fuel Cell Store], ultra-pure DIW (10 g, 18.2 MΩ cm, Milli-Q), 5 wt% PiperION (0.4 g) [Versogen], and isopropyl alcohol (34 g), in that

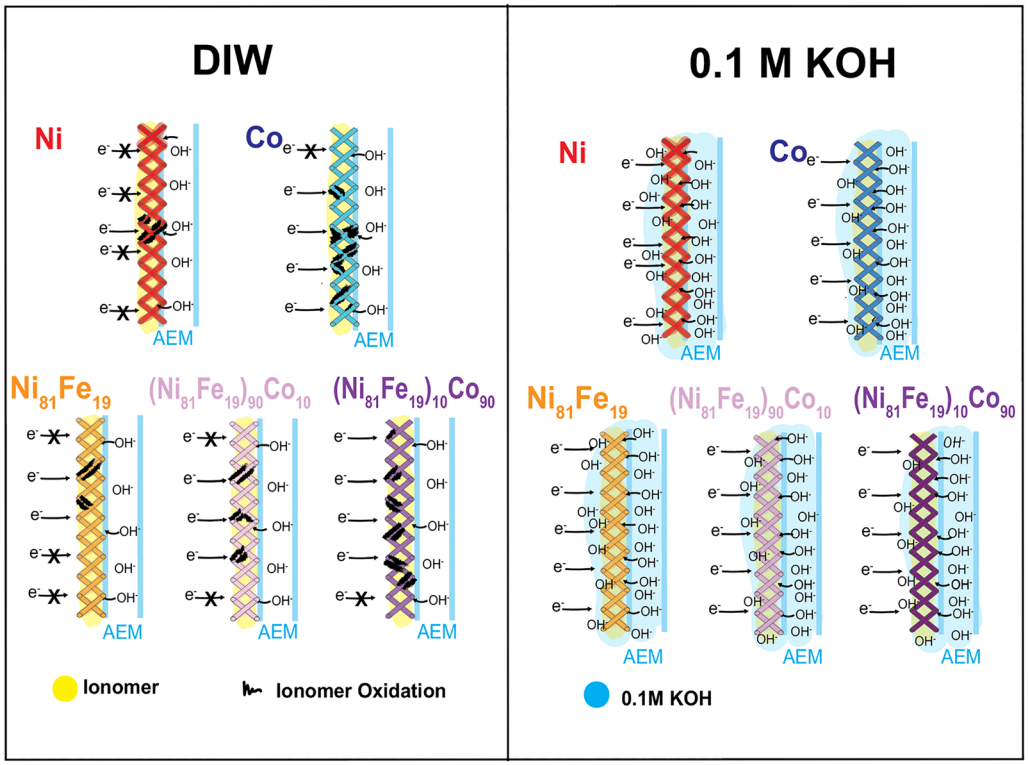

Fig. 6 Schematic illustration of ionomer degradation and performance trends in anode catalyst layers under different electrolyte conditions. Representation of Ni, Co, $Ni_{81}Fe_{19}$, $(Ni_{81}Fe_{19})_{90}Co_{10}$, and $(Ni_{81}Fe_{19})_{10}Co_{90}$ anode interfaces in AEMWE operated with ultra-pure deionized water (DIW, left) and 0.1 M KOH (right). Yellow regions indicate the ionomer layer, black wavy marks denote ionomer oxidation, and blue shading represents the presence of 0.1 M KOH electrolyte. Arrows show electron and hydroxide transport pathways across the catalyst–ionomer AEM interface.

order.[40,64] Adding water to the catalyst particles prior to isopropyl alcohol is critical in reducing the risk of fire. The mixture was transferred to a Falcon tube and bath sonicated (Branson) for a minimum of 2 hours until the ink was fully dispersed. 120 wet-proof Toray carbon PTL (Fuel Cell Store) was cut into desired dimensions and taped onto the Sonotek spray coater hot plate (80 °C), with the front corners secured to ensure stability. The Sonotek settings were as follows: shaping air 0.4 psi, flow rate 1, nozzle power 2, and line speed 60 mm s^{-1}. Spraying was performed in a serpentine pattern to ensure full coverage. To weigh the catalyst mass between sprays, the tape frame was removed, and the electrodes were allowed to cool down to room temperature before weighing. This process was repeated until the desired loading of 2 ± 0.1 mg cm^{-2} was reached. After the catalyst was hand-sprayed using an Airbrush (Testors, A220) at 10 PSI, a 2 wt% PiperION solution was applied over the catalyst layer in a pulsed serpentine pattern until the ionomer overlayer reached 10%–20% of the catalyst mass. For a detailed description of similar preparation methods, the reader is pointed to our recent protocol.[40]

4.1.2. Anode preparation. Thin film metal samples were prepared *via* a custom-made electron beam PVD vacuum chamber (Technical Engineering Services). Metal pellets (Co 99.95%, Ni 99.95%, $Ni_{81}Fe_{19}$ 99.95%) and crucibles were purchased from Kurt J. Lesker. Co, Ni, and $Ni_{81}Fe_{19}$ were deposited *via* electron beam induced metal evaporation. For NiFeCo alloys, $Ni_{81}Fe_{19}$ and Co were co-deposited. In each case, a 100 nm catalyst layer was deposited onto a stainless steel (25AL3, Bekaert) porous transport layer (PTL) with a deposition rate of 0.1–2.0 Å s^{-1} as measured with a quartz crystal microbalance. After deposition, the thin-film catalysts were dip-coated by horizontally dipping the catalyst side of the PTL into the ionomer solution (2 wt% PiperION in EtOH) and then dried on a hot plate at 80 °C. The ionomer topcoat loading was calculated from the mass difference of PTLs before and after dip coating, resulting in an ionomer overlayer of approximately 1.0 ± 0.3 mg cm^{-2}. To compare our thin-film anodes to more widely used AEM anodes, we also spray-coated 2.5–2.7 mg cm^{-2} IrO_x (fuel cell store) nanoparticles on the same stainless steel PTL in a similar manner as described above for the cathode.

4.1.3. Membrane preparation. 40 μm thick PiperION TP-85 membranes (Versogen) were pretreated by soaking in 0.5 M KOH for 2 hours, followed by replacement with fresh 0.5 M KOH to ensure complete ion exchange following the manufacturer's instructions. Membranes were stored in 0.5 M KOH at room temperature when not in use for a maximum of 2 weeks. Membranes were washed with ultrapure DI water (DIW) before assembly in the electrolyzers.

4.2. MEA preparation

Electrodes were cut to 1 cm^2 and assembled in the electrolyzer, similar to published procedures.[13] Glass reservoirs (one for the

anode, one for the cathode) were filled with either 0.1 M KOH (Thermo Fisher, Trace Metal Grade, 99.99%) or 18.2 MΩ ultrapure DI water (DIW), and diaphragm pumps (KNF) were used to supply liquid to the cathode and anode at 60 mL min^{-1} through polyethylene tubing (0.250 in outer diameter, 0.170 in inner diameter). The water and KOH were preheated to 70 ± 1 °C *via* hotplates under the glass reservoirs and adjusted to ensure a cell temperature of 50 ± 1 °C, as monitored with a k-type thermocouple inserted into the cathode cell hardware plate.

A Ti plate was used as a rigid back support on both the cathode and anode side (400 μm thickness, Baoji Yingao Metal Materials Inc.). Gasket material (0.005 in. and 0.01 in. PTFE/PETE film, McMaster-Carr) was laser cut (Universal, PLS 6.120) to an active area of 1 cm^2. PTFE is preferred for experiments in KOH due to increased durability. Based on previous literature,[49] we used a total of 0.035 in of gasket on the anode and 0.030 in on the cathode. Lastly, a torque wrench was used to tighten the screws in a star pattern first to 2.4 N-m, followed by final tightening to 5.6 N-m.

4.3. Electrolysis procedure

The MEA was conditioned by increasing the current density from 100 mA cm^{-2} to 1 A cm^{-2}, in 100 mA cm^{-2} increments, holding for 2 min at each step. The current was then decreased in 50 mA cm^{-2} steps, measuring the potential for 10 s at each step to collect the *J–V* curve before increasing the current density from 50 mA cm^{-2} to 1 A cm^{-2} in 50 mA cm^{-2} increments for 20 s steps. We will describe this protocol as 'break-in' as it promotes catalyst activation, full hydration of the membrane/ionomer, and establishment of stable ionic pathways.[13,22,49] The cell was held at 1 A cm^{-2} for 24 hours for stability measurements. Galvanostatic electrochemical impedance spectroscopy (GEIS) was conducted at 1 A cm^{-2} with a 50 mA cm^{-2} sinusoidal modulation from 1 MHz to 100 mHz before and after stability testing at 1 A cm^{-2}. After analysis, the cells were disassembled, and the ionomer and membrane were soaked in 3.0 M NaCl to ion exchange OH^- by Cl^- in order to prevent additional ionomer degradation *via* OH^- attack during drying of the ionomer.[38]

4.4. Characterization techniques

4.4.1. XPS, XRD, and SEM analysis. X-ray diffraction patterns were collected using a Bruker D8 Venture diffractometer in grazing incidence geometry with an incident angle between 5° and 8°, employing Mo Kα radiation (0.71 Å). XPS measurements were performed using a PHI Versa Probe 4 system equipped with a monochromatic Al Kα source (1486.4 eV) and a 200 μm spot size. Charge neutralization was achieved using both Ar^+ and electron flood guns. All spectra were referenced to the adventitious C 1s peak at 284.8 eV. Depth profiles were obtained by applying a 5 kV Ar^+ ion beam for 2-minute etching intervals between measurements. CASA XPS software was used to quantify atomic ratios, with Ni and Fe concentrations determined from the Ni 3p and Fe 3p peaks to avoid overlap between Ni Auger signals and the Fe $2p_{3/2}$ region. C 1s, N 1s, and F 1s peaks were analyzed to assess ionomer chemical changes and oxidative degradation. Phenom desktop SEM at the SLAC Shared Facilities was used to characterize samples prior to experimentation and to perform elemental analysis using energy-dispersive X-ray spectroscopy (EDX) to confirm the presence of catalysts after PVD deposition. The electron beam was operated at an accelerating voltage of 10 kV.

4.4.2. ICP-MS. Metal dissolution into the anolyte was quantified using an inductively coupled plasma mass spectrometer (ICP-MS, Thermo Scientific iCAP RQ) equipped with an auto-sampler and operated in helium kinetic energy discrimination (He-KED) mode to minimize polyatomic interferences. Samples were acidified to 2% v/v with trace-metal grade nitric acid (Fisher Scientific) immediately after collection and stored in acid-washed polypropylene tubes prior to analysis. Calibration standards for Ni, Fe, Co, and Cr were prepared by serial dilution of 1000 ppm single-element standards (Ricca Chemical) to generate a 0–500 ppb calibration range.

Author contributions

B. M. R. M. contributed to conceptualization, data curation, formal analysis, investigation, methodology, visualization, writing – original draft, and writing – review & editing. R. T. H. contributed to conceptualization, formal analysis, investigation, and writing – review & editing. S. K. contributed to investigation, methodology, and writing – review & editing. C. F. C. contributed to investigation, methodology, and writing – review & editing. A. V. contributed to investigation, methodology, and writing – review & editing. A. M. A. contributed to investigation, methodology, and writing – review & editing. J. S. contributed to conceptualization and writing – review & editing. D. H. M. contributed to conceptualization and writing – review & editing. I. R. A. contributed to conceptualization and writing – review & editing. J. S. contributed to writing – review & editing. A. C. N. contributed to conceptualization, supervision, funding acquisition, and writing – review & editing. M. B. S. contributed to conceptualization, methodology, supervision, funding acquisition, and writing – review & editing. T. F. J. contributed to resources, supervision, funding acquisition, writing – original draft, and writing – review & editing.

Conflicts of interest

There are no conflicts of interest to declare.

Data availability

Data supporting this study are available within the article and the associated supplementary information (SI). Supplementary information is available. See DOI: https://doi.org/10.1039/d6ey00058d.

Acknowledgements

This research was supported by the U.S. Department of Energy, Office of Science, Office of Basic Energy Sciences, Chemical Sciences, Geosciences, and Biosciences Division, Catalysis

Science Program to the SUNCAT Center for Interface Science and Catalysis. B. M. R. M. acknowledges the Stanford Graduate Fellowship, RAISE Fellowship, and GEM Fellowship. J. S. acknowledges the Leopoldina postdoc fellowship program (grant number LPDS 2022-02) of the German National Academy of Sciences Leopoldina. DHM acknowledges the TomKat Center for Sustainable Energy Fellowship for Translational Research. Partial support for research materials and electrolyzer fabrication was provided by the Office of Naval Research, grant N00014-24-1-2433. I.R.A and A. V. acknowledge support from the National Science Foundation Graduate Research Fellowship (grant number under Grant No. DGE-2146755) and from the Stanford Graduate Fellowship *via* the Leonard J. Shustek Award.

References

1 T.-Z. Ang, M. Salem, M. Kamarol, H. S. Das, M. A. Nazari and N. Prabaharan, A Comprehensive Study of Renewable Energy Sources: Classifications, Challenges and Suggestions, *Energy Strategy Rev*, 2022, **43**, 100939, DOI: 10.1016/j.esr.2022.100939.

2 S. Kharel and B. Shabani, Hydrogen as a Long-Term Large-Scale Energy Storage Solution to Support Renewables, *Energies*, 2018, **11**(10), 2825, DOI: 10.3390/en11102825.

3 M. Schalenbach, A. R. Zeradjanin, O. Kasian, S. Cherevko and K. J. J. Mayrhofer, A Perspective on Low-Temperature Water Electrolysis – Challenges in Alkaline and Acidic Technology, *Int. J. Electrochem. Sci.*, 2018, **13**(2), 1173–1226, DOI: 10.20964/2018.02.26.

4 K. Ayers, N. Danilovic, R. Ouimet, M. Carmo, B. Pivovar and M. Bornstein, Perspectives on Low-Temperature Electrolysis and Potential for Renewable Hydrogen at Scale, *Annu. Rev. Chem. Biomol. Eng.*, 2019, **10**, 219–239, DOI: 10.1146/annurev-chembioeng-060718-030241.

5 M. E. Şahin, An Overview of Different Water Electrolyzer Types for Hydrogen Production, *Energies*, 2024, **17**(19), 4944, DOI: 10.3390/en17194944.

6 A. W. Tricker, J. K. Lee, J. R. Shin, N. Danilovic, A. Z. Weber and X. Peng, Design and Operating Principles for High-Performing Anion Exchange Membrane Water Electrolyzers, *J. Power Sources*, 2023, **567**, 232967, DOI: 10.1016/j.jpowsour.2023.232967.

7 M. Bodner, A. Hofer and V. Hacker, H2 Generation from Alkaline Electrolyzer, *Wiley Interdiscip. Rev.: Energy Environ.*, 2015, **4**(4), 365–381, DOI: 10.1002/wene.150.

8 C. Santoro, A. Lavacchi, P. Mustarelli, V. Di Noto, L. Elbaz, D. R. Dekel and F. Jaouen, What Is Next in Anion-Exchange Membrane Water Electrolyzers? Bottlenecks, Benefits, and Future, *ChemSusChem*, 2022, **15**(8), e202200027, DOI: 10.1002/cssc.202200027.

9 C. V. Pham, D. Escalera-López, K. Mayrhofer, S. Cherevko and S. Thiele, Essentials of High Performance Water Electrolyzers – From Catalyst Layer Materials to Electrode Engineering, *Adv. Energy Mater.*, 2021, **11**(44), 2101998, DOI: 10.1002/aenm.202101998.

10 A. R. Zeradjanin, A. A. Topalov, Q. Van Overmeere, S. Cherevko, X. X. Chen, E. Ventosa, W. Schuhmannc and K. J. J. Mayrhofer, Rational Design of the Electrode Morphology for Oxygen Evolution – Enhancing the Performance for Catalytic Water Oxidation, *RSC Adv.*, 2014, **4**, 9579–9587.

11 S. Cherevko, Stability and Dissolution of Electrocatalysts: Building the Bridge between Model and "Real World" Systems, *Curr. Opin. Electrochem.*, 2018, **8**, 118–125, DOI: 10.1016/j.coelec.2018.03.034.

12 R. A. Marquez, M. Espinosa, E. Kalokowski, Y. J. Son, K. Kawashima, T. V. Le, C. E. Chukwuneke and C. B. Mullins, A Guide to Electrocatalyst Stability Using Lab-Scale Alkaline Water Electrolyzers, *ACS Energy Lett*, 2024, **9**(2), 547–555, DOI: 10.1021/acsenergylett.3c02758.

13 G. A. Lindquist, S. Z. Oener, R. Krivina, A. R. Motz, A. Keane, C. Capuano, K. E. Ayers and S. W. Boettcher, Performance and Durability of Pure-Water-Fed Anion Exchange Membrane Electrolyzers Using Baseline Materials and Operation, *ACS Appl. Mater. Interfaces*, 2021, **13**(44), 51917–51924, DOI: 10.1021/acsami.1c06053.

14 L. N. Stanislaw, M. R. Gerhardt and A. Z. Weber, Modeling Electrolyte Composition Effects on Anion-Exchange-Membrane Water Electrolyzer Performance, *ECS Trans*, 2019, **92**(8), 767, DOI: 10.1149/09208.0767ecst.

15 J. Liu and A. Z. Weber, Ionomer Optimization for Hydroxide-Exchange-Membrane Water Electrolyzers Operated with Distilled Water: A Modeling Study, *J. Electrochem. Soc.*, 2022, **169**(5), 054506, DOI: 10.1149/1945-7111/ac69c4.

16 S. Karim, N. Tanwar, S. Das, R. Ranjit, A. Banerjee, G. Gulafshan, A. Gupta, A. Kumar and A. Dutta, Shaping the Future of Green Hydrogen Production: Overcoming Conventional Challenges with Molecular Catalysts, Immobilization, and Scalable Electrolyzers, *ACS Catal*, 2025, **15**(2), 1073–1096, DOI: 10.1021/acscatal.4c05986.

17 E. Potvin and L. Brossard, Electrocatalytic Activity of Ni-Fe Anodes for Alkaline Water Electrolysis, *Mater. Chem. Phys.*, 1992, **31**(4), 311–318, DOI: 10.1016/0254-0584(92)90192-B.

18 R. A. Marquez, E. Kalokowski, M. Espinosa, J. T. Bender, Y. J. Son, K. Kawashima, C. E. Chukwuneke, L. A. Smith, H. Celio, A. Dolocan, X. Zhan, N. Miller, D. J. Milliron, J. Resasco and C. B. Mullins, Transition Metal Incorporation: Electrochemical, Structure, and Chemical Composition Effects on Nickel Oxyhydroxide Oxygen-Evolution Electrocatalysts, *Energy Environ. Sci.*, 2024, **17**, 2028–2045.

19 J. Deng, M. R. Nellist, M. B. Stevens, C. Dette, Y. Wang and S. W. Boettcher, Morphology Dynamics of Single-Layered Ni(OH)2/NiOOH Nanosheets and Subsequent Fe Incorporation Studied by in Situ Electrochemical Atomic Force Microscopy, *Nano Lett*, 2017, **17**(11), 6922–6926, DOI: 10.1021/acs.nanolett.7b03313.

20 M. S. Burke, M. G. Kast, L. Trotochaud, A. M. Smith and S. W. Boettcher, Cobalt–Iron (Oxy)Hydroxide Oxygen Evolution Electrocatalysts: The Role of Structure and Composition on Activity, Stability, and Mechanism, *J. Am. Chem. Soc.*, 2015, **137**(10), 3638–3648, DOI: 10.1021/jacs.5b00281.

21 D. Xu, M. B. Stevens, M. R. Cosby, S. Z. Oener, A. M. Smith, L. J. Enman, K. E. Ayers, C. B. Capuano, J. N. Renner, N. Danilovic, Y. Li, H. Wang, Q. Zhang and S. W. Boettcher, Earth-Abundant Oxygen Electrocatalysts for Alkaline Anion-Exchange-Membrane Water Electrolysis: Effects of Catalyst Conductivity and Comparison with Performance in Three-Electrode Cells, *ACS Catal*, 2019, **9**(1), 7–15, DOI: 10.1021/acscatal.8b04001.

22 R. A. Krivina, G. A. Lindquist, M. C. Yang, A. K. Cook, C. H. Hendon, A. R. Motz, C. Capuano, K. E. Ayers, J. E. Hutchison and S. W. Boettcher, Three-Electrode Study of Electrochemical Ionomer Degradation Relevant to Anion-Exchange-Membrane Water Electrolyzers, *ACS Appl. Mater. Interfaces*, 2022, **14**(16), 18261–18274, DOI: 10.1021/acsami.1c22472.

23 I. R. Amador, R. T. Hannagan, A. Qiang, S.-W. Lee, N. T. T. Tran, K. M. K. Yap, A. M. Aleman, D. H. Marin, M. R. Mendoza, M. B. Stevens, T. F. Jaramillo and A. C. Nielander, Diagnosing Mechanisms to Mitigate Anion Exchange Ionomer Degradation during Impure Water Electrolysis, *Energy Environ. Sci.*, 2025, **18**, 10195–10204, DOI: 10.1039/D5EE03891J.

24 L. J. Titheridge and A. T. Marshall, The Rationale for a Standardized Testing Protocol for Anion Exchange Membrane Water Electrolyzers, *ACS Energy Lett.*, 2024, **9**(3), 1288–1294, DOI: 10.1021/acsenergylett.4c00239.

25 Z. Wang, L. Xin, X. Zhao, Y. Qiu, Z. Zhang, O. A. Baturina and W. Li, Carbon Supported Ag Nanoparticles with Different Particle Size as Cathode Catalysts for Anion Exchange Membrane Direct Glycerol Fuel Cells, *Renewable Energy*, 2014, **62**, 556–562, DOI: 10.1016/j.renene.2013.08.005.

26 K. Yu, D. J. Groom, X. Wang, Z. Yang, M. Gummalla, S. C. Ball, D. J. Myers and P. J. Ferreira, Degradation Mechanisms of Platinum Nanoparticle Catalysts in Proton Exchange Membrane Fuel Cells: The Role of Particle Size, *Chem. Mater.*, 2014, **26**(19), 5540–5548, DOI: 10.1021/cm501867c.

27 D. K. Murugaiah and S. Shahgaldi, Recent Progress in Understanding the Dispersion Stability of Catalyst Ink for Proton Exchange Membrane Fuel Cell and Water Electrolyzer, *Int. J. Hydrogen Energy*, 2024, **66**, 156–169, DOI: 10.1016/j.ijhydene.2024.04.036.

28 C. Han, W. Shi, M. Huang, Q. Wang, J. Yang, J. Chen, R. Ding and X. Yin, Solvent Effects on the Catalyst Ink and Layer Microstructure for Anion Exchange Membrane Fuel Cells, *ACS Appl. Mater. Interfaces*, 2024, **16**(4), 4550–4560, DOI: 10.1021/acsami.3c14404.

29 W.-J. Choi, I. Kang, D. M. Yu, S. J. Yoon, S. So and K.-H. Oh, Effect of Catalyst Ink Properties on the Performance of Proton Exchange Membrane Fuel Cell and Water Electrolyzer: A Mini Review, *Korean J. Chem. Eng*, 2024, **42**, 3459–3470, DOI: 10.1007/s11814-024-00221-2.

30 B. Britton and S. Holdcroft, The Control and Effect of Pore Size Distribution in AEMFC Catalyst Layers, *J. Electrochem. Soc.*, 2016, **163**(5), F353, DOI: 10.1149/2.0421605jes.

31 A. Y. Faid, L. Xie, A. O. Barnett, F. Seland, D. Kirk and S. Sunde, Effect of Anion Exchange Ionomer Content on Electrode Performance in AEM Water Electrolysis, *Int. J. Hydrogen Energy*, 2020, **45**(53), 28272–28284, DOI: 10.1016/j.ijhydene.2020.07.202.

32 E. K. Volk, A. L. Clauser, M. E. Kreider, D. D. Soetrisno, S. Khandavalli, J. D. Sugar, S. Kwon and S. M. Alia, Role of the Ionomer in Supporting Electrolyte-Fed Anion Exchange Membrane Water Electrolyzers, *ACS Electrochem*, 2024, **1**(2), 239–248, DOI: 10.1021/acselectrochem.4c00061.

33 M. E. Kreider, H. Yu, L. Osmieri, M. R. Parimuha, K. S. Reeves, D. H. Marin, R. T. Hannagan, E. K. Volk, T. F. Jaramillo, J. L. Young, P. Zelenay and S. M. Alia, Understanding the Effects of Anode Catalyst Conductivity and Loading on Catalyst Layer Utilization and Performance for Anion Exchange Membrane Water Electrolysis, *ACS Catal.*, 2024, **14**(14), 10806–10819, DOI: 10.1021/acscatal.4c02932.

34 M. B. Stevens, L. J. Enman, A. S. Batchellor, M. R. Cosby, A. E. Vise, C. D. M. Trang and S. W. Boettcher, Measurement Techniques for the Study of Thin Film Heterogeneous Water Oxidation Electrocatalysts, *Chem. Mater.*, 2017, **29**(1), 120–140, DOI: 10.1021/acs.chemmater.6b02796.

35 S. Klaus, M. W. Louie, L. Trotochaud and A. T. Bell, Role of Catalyst Preparation on the Electrocatalytic Activity of Ni1–xFexOOH for the Oxygen Evolution Reaction, *J. Phys. Chem. C*, 2015, **119**(32), 18303–18316, DOI: 10.1021/acs.jpcc.5b04776.

36 A. M. Aleman, C. F. Crago, A. Vargas, C. H. Reyes, H. O. Badr, J. Zander, A. S. Mule, R. T. Hannagan, O. A. Oriowo, B. M. R. Mendoza, M. B. Stevens and T. F. Jaramillo, Insights into the Acid Stability of Cobalt Electrocatalysts *via* Time-Resolved Activity-Durability Relationships for Tailored Bimetallic Thin Films, *Adv. Energy Mater.*, 2026, **16**(6), e04936, DOI: 10.1002/aenm.202504936.

37 C. Lei, K. Yang, G. Wang, G. Wang, J. Lu, L. Xiao and L. Zhuang, Impact of Catalyst Reconstruction on the Durability of Anion Exchange Membrane Water Electrolysis, *ACS Sustain. Chem. Eng.*, 2022, **10**(50), 16725–16733, DOI: 10.1021/acssuschemeng.2c04855.

38 R. A. Krivina, G. A. Lindquist, S. R. Beaudoin, T. N. Stovall, W. L. Thompson, L. P. Twight, D. Marsh, J. Grzyb, K. Fabrizio, J. E. Hutchison and S. W. Boettcher, Anode Catalysts in Anion-Exchange-Membrane Electrolysis without Supporting Electrolyte: Conductivity, Dynamics, and Ionomer Degradation, *Adv. Mater.*, 2022, **34**(35), 2203033, DOI: 10.1002/adma.202203033.

39 M. Mattinen, J. Schröder, G. D'Acunto, M. Ritala, T. F. Jaramillo, M. B. Stevens and S. F. Bent, Dynamics of Precatalyst Conversion and Iron Incorporation in Nickel-Based Alkaline Oxygen Evolution Reaction Catalysts, *Cell Rep. Phys. Sci*, 2024, **5**(11), 102284, DOI: 10.1016/j.xcrp.2024.102284.

40 I. Rios Amador, R. T. Hannagan, D. H. Marin, J. T. Perryman, C. Rémy, M. A. Hubert, G. A. Lindquist, L. Chen, M. B. Stevens, S. W. Boettcher, A. C. Nielander and T. F. Jaramillo, Protocol for Assembling and Operating Bipolar Membrane Water Electrolyzers, *STAR Protoc*, 2023, **4**(4), 102606, DOI: 10.1016/j.xpro.2023.102606.

41 R. L. Doyle, I. J. Godwin, M. P. Brandon and M. E. G. Lyons, Redox and Electrochemical Water Splitting Catalytic Properties of Hydrated Metal Oxide Modified Electrodes, *Phys. Chem. Chem. Phys.*, 2013, **15**(33), 13737–13783, DOI: 10.1039/C3CP51213D.

42 E. B. Ferreira and G. Jerkiewicz, On the Electrochemical Reduction of β-Ni(OH)2 to Metallic Nickel, *Electrocatalysis*, 2021, **12**(2), 199–209, DOI: 10.1007/s12678-021-00643-0.

43 A. V. Ven, D. der; Morgan, Y. S. Meng and G. Ceder, Phase Stability of Nickel Hydroxides and Oxyhydroxides, *J. Electrochem. Soc.*, 2005, **153**(2), A210, DOI: 10.1149/1.2138572.

44 S. Hou, A. Sekar, Y. Zhao, M. Kwak, J. Oh, K. K.-Y. Li, P. Wu, R. T. Hannagan, V. Cartagena, A. C. Ekennia, H. Duan, M. J. Zachman, J. Frechette, G. M. Su, B. Lakshmanan, Y. Yan, T. F. Jaramillo and S. W. Boettcher, Durable, Pure Water–Fed, Anion-Exchange Membrane Electrolyzers through Interphase Engineering, *Science*, 2025, **390**(6770), 294–298, DOI: 10.1126/science.adw7100.

45 T. Priamushko, E. Franz, A. Logar, L. Bijelić, P. Guggenberger, D. Escalera-López, M. Zlatar, J. Libuda, F. Kleitz, N. Hodnik, O. Brummel and S. Cherevko, Be Aware of Transient Dissolution Processes in Co3O4 Acidic Oxygen Evolution Reaction Electrocatalysts, *J. Am. Chem. Soc.*, 2025, **147**(4), 3517–3528, DOI: 10.1021/jacs.4c14952.

46 A. M. Aleman, C. F. Crago, G. A. Kamat, A. S. Mule, J. E. Avilés Acosta, J. E. Matthews, N. Keyes, R. T. Hannagan, A. C. Nielander, M. B. Stevens and T. F. Jaramillo, Multimodal In Situ Characterization Uncovers Unexpected Stability of a Cobalt Electrocatalyst for Acidic Sustainable Energy Technologies, *J. Am. Chem. Soc.*, 2025, **147**(12), 10309–10319, DOI: 10.1021/jacs.4c16707.

47 G. A. Lindquist, J. C. Gaitor, W. L. Thompson, V. Brogden, K. J. T. Noonan and S. W. Boettcher, Oxidative Instability of Ionomers in Hydroxide-Exchange-Membrane Water Electrolyzers, *Energy Environ. Sci.*, 2023, **16**(10), 4373–4387, DOI: 10.1039/D3EE01293J.

48 D. S. Maxwell, I. Kendrick and S. Mukerjee, Operando Raman Spectroscopy Reveals Degradation Byproducts from Ionomer Oxidation in Anion Exchange Membrane Water Electrolyzers, *J. Am. Chem. Soc.*, 2024, **146**(32), 22431–22444, DOI: 10.1021/jacs.4c05721.

49 Q. Xu, S. Z. Oener, G. Lindquist, H. Jiang, C. Li and S. W. Boettcher, Integrated Reference Electrodes in Anion-Exchange-Membrane Electrolyzers: Impact of Stainless-Steel Gas-Diffusion Layers and Internal Mechanical Pressure, *ACS Energy Lett*, 2021, **6**(2), 305–312, DOI: 10.1021/acsenergylett.0c02338.

50 M. T. de Groot and P. Vermeulen, Advanced Characterization of Alkaline Water Electrolysis through Electrochemical Impedance Spectroscopy and Polarization Curves, *J. Electroanal. Chem.*, 2024, **974**, 118709, DOI: 10.1016/j.jelechem.2024.118709.

51 L. Zhang, Q. Xu, Y. Hu, L. Chen and H. Jiang, Benchmarking the pH–Stability Relationship of Metal Oxide Anodes in Anion Exchange Membrane Water Electrolysis, *ACS Sustain. Chem. Eng.*, 2023, **11**(36), 13251–13259, DOI: 10.1021/acssuschemeng.3c01619.

52 S. Senthil, V. Ratchagar, T. Thangeeswari, S. Srinivasan and R. Murugan, Impact of pH Levels on the Morphological, Dielectric and Impedance Spectral Behaviour of Cobalt Oxide Nanomaterials, *Dig. J. Nanomater. Biostructures*, 2023, **18**(4), 1235–1247, DOI: 10.15251/DJNB.2023.184.1235.

53 F. Yang, X. Zhou, N. T. Plymale, K. Sun and N. S. Lewis, Evaluation of Sputtered Nickel Oxide, Cobalt Oxide and Nickel–Cobalt Oxide on n-Type Silicon Photoanodes for Solar-Driven O2(g) Evolution from Water, *J. Mater. Chem. A*, 2020, **8**(28), 13955–13963, DOI: 10.1039/D0TA03725G.

54 Y. Xia, Y. Yang and H. Shao, Differences in the Effects of Co and CoO on the Performance of Ni(OH)2 Electrode in Ni/MH Power Battery, *J. Power Sources*, 2011, **196**(1), 495–503, DOI: 10.1016/j.jpowsour.2010.06.065.

55 M. B. Stevens, L. J. Enman, E. H. Korkus, J. Zaffran, C. D. M. Trang, J. Asbury, M. G. Kast, M. C. Toroker and S. W. Boettcher, Ternary Ni-Co-Fe Oxyhydroxide Oxygen Evolution Catalysts: Intrinsic Activity Trends, Electrical Conductivity, and Electronic Band Structure, *Nano Res*, 2019, **12**(9), 2288–2295, DOI: 10.1007/s12274-019-2391-y.

56 J. Liu, Z. Kang, D. Li, M. Pak, S. M. Alia, C. Fujimoto, G. Bender, Y. S. Kim and A. Z. Weber, Elucidating the Role of Hydroxide Electrolyte on Anion-Exchange-Membrane Water Electrolyzer Performance, *J. Electrochem. Soc.*, 2021, **168**(5), 054522, DOI: 10.1149/1945-7111/ac0019.

57 I. Vincent, E.-C. Lee and H.-M. Kim, Comprehensive Impedance Investigation of Low-Cost Anion Exchange Membrane Electrolysis for Large-Scale Hydrogen Production, *Sci. Rep.*, 2021, **11**(1), 293, DOI: 10.1038/s41598-020-80683-6.

58 N. U. Hassan, Y. Zheng, P. A. Kohl and W. E. Mustain, KOH vs Deionized Water Operation in Anion Exchange Membrane Electrolyzers, *J. Electrochem. Soc.*, 2022, **169**(4), 044526, DOI: 10.1149/1945-7111/ac5f1d.

59 A. Y. Faid, A. O. Barnett, F. Seland and S. Sunde, Ternary NiCoFe Nanosheets for Oxygen Evolution in Anion Exchange Membrane Water Electrolysis, *Int. J. Hydrogen Energy*, 2022, **47**(56), 23483–23497, DOI: 10.1016/j.ijhydene.2022.05.143.

60 L. Trotochaud, J. K. Ranney, K. N. Williams and S. W. Boettcher, Solution-Cast Metal Oxide Thin Film Electrocatalysts for Oxygen Evolution, *J. Am. Chem. Soc.*, 2012, **134**(41), 17253–17261, DOI: 10.1021/ja307507a.

61 B. Tian, H. Shin, S. Liu, M. Fei, Z. Mu, C. Liu, Y. Pan, Y. Sun, W. A. Goddard and M. Ding, Double-Exchange-Induced in Situ Conductivity in Nickel-Based Oxyhydroxides: An Effective Descriptor for Electrocatalytic Oxygen Evolution, *Angew. Chem., Int. Ed.*, 2021, **60**, 16448, DOI: 10.1002/anie.202101906.

62 J. T. Mefford, A. R. Akbashev, M. Kang, C. L. Bentley, W. E. Gent, H. D. Deng, D. H. Alsem, Y.-S. Yu, N. J. Salmon, D. A. Shapiro, P. R. Unwin and W. C. Chueh, Correlative Operando Microscopy of Oxygen Evolution Electrocatalysts, *Nature*, 2021, **593**(7857), 67–73, DOI: 10.1038/s41586-021-03454-x.

63 Q. Li, A. Molina Villarino, C. R. Peltier, A. J. Macbeth, Y. Yang, M.-J. Kim, Z. Shi, M. R. Krumov, C. Lei, G. G. Rodríguez-Calero, J. Soto, S.-H. Yu, P. F. Mutolo, L. Xiao, L. Zhuang, D. A. Muller, G. W. Coates, P. Zelenay and H. D. Abruña, Anion Exchange Membrane Water Electrolysis: The Future of Green Hydrogen, *J. Phys. Chem. C*, 2023, **127**(17), 7901–7912, DOI: 10.1021/acs.jpcc.3c00319.

64 D. H. Marin, J. T. Perryman, M. A. Hubert, G. A. Lindquist, L. Chen, A. M. Aleman, G. A. Kamat, V. A. Niemann, M. B. Stevens, Y. N. Regmi, S. W. Boettcher, A. C. Nielander and T. F. Jaramillo, Hydrogen Production with Seawater-Resilient Bipolar Membrane Electrolyzers, *Joule*, 2023, **7**(4), 765–781, DOI: 10.1016/j.joule.2023.03.005.